Short Communication
doi.org/10.1002/elsa.202100068

Chemistry Europe
European Chemical Societies Publishing

Received: 16 April 2021
Revised: 2 July 2021
Accepted: 20 July 2021

Lithium intercalation into graphite: In operando analysis of Raman signal widths

Sven Jovanovic[1,2] | **Peter Jakes**[1] | **Steffen Merz**[1] | **Rüdiger-A. Eichel**[1,3] | **Josef Granwehr**[1,2]

[1] Forschungszentrum Jülich, Institute of Energy and Climate Research, Fundamental Electrochemistry (IEK-9), Jülich, Germany

[2] Institute of Technical and Macromolecular Chemistry, RWTH Aachen University, Aachen, Germany

[3] Institute of Physical Chemistry, RWTH Aachen University, Aachen, Germany

Correspondence
Sven Jovanovic, Forschungszentrum Jülich, Institute of Energy and Climate Research, Fundamental Electrochemistry (IEK-9), Jülich, Germany.
Email: s.jovanovic@fz-juelich.de

Funding information
Bundesministerium für Bildung und Forschung, Grant/Award Number: 03XP0352

Abstract

The mechanism of reversible lithium intercalation in graphite anodes is still not fully understood. In operando Raman spectroscopy provides a sensitive means to monitor structural changes during the intercalation process. Analysis of the D-band to G-band intensity ratio (D/G ratio) is a common method to study the structure of carbon materials. However, this approach is complicated for the investigation of graphite anodes during battery cycling, as the D-band disappears with the onset of lithium intercalation. To circumvent this issue, the D/G ratio can be replaced by using the G-band full-width-at-half-maximum (FWHM). In this study, an investigation of the G-band FWHM during battery cell cycling is demonstrated as an alternative to monitor the intercalation of lithium into a graphite electrode. It was observed that lithium intercalation already occurs to a small extent during solid–electrolyte interphase (SEI) formation and that the formation of staged intercalation compounds leads to a continuous deformation of the boundary graphene layer.

KEYWORDS
graphite, in operando, intercalation, lithium-ion batteries, Raman spectroscopy

1 | INTRODUCTION

In lithium-ion batteries (LIBs) graphite is commonly used as anode material. During battery operation, lithium ions are reversibly intercalated into the graphite lattice.[1–3] It is suggested that the onset of lithium intercalation can be described as a statistic insertion of ions into the lattice, which is known as dilute stage-1.[4] For higher lithium concentrations in graphite, intercalation proceeds as a staging process, where several staged graphite intercalation compounds (GICs) are formed. These GICs are defined by the number of graphene layers that separate the intercalated lithium ions. The GIC formations start as stage-4 compound (LiC_{24}), whereas the lattice is fully intercalated when a stage-1 compound (LiC_6) is achieved.[5,6] The underlying details of the intercalation mechanisms have been studied using computational calculations and various experimental techniques such as XRD, Raman, and NMR spectroscopy.[7–9] Nevertheless, the mechanism is not yet fully understood.[10]

Raman spectroscopy is a powerful method for the research on carbon materials ex situ and in operando. Studies employing Raman spectroscopy are a major contribution to the investigation of the intercalation process of

Short Communication
doi.org/10.1002/elsa.202100068
Chemistry Europe
European Chemical Societies Publishing

lithium in graphite.[11] In general, the Raman spectrum of graphite consists of the G-band band (1580 cm^{-1}), arising from C-C bond stretching of the sp^2-bonded carbon, the D-band (ca. 1350 cm^{-1}), which appears in case of a defective lattice, and the double-resonance 2D-band (ca. 2700 cm^{-1}), which is present independently of lattice defects.[12,13] During the lithium intercalation process, the G-band is subject to major evolutions and can thus be employed to determine the progress of the staging process.[5,11,14–16] In a more recent study, Sole *et al.* monitored changes in the 2D band and suggested an intercalation in a staggered fashion, which causes a strong deformation of the graphene layers.[8]

For ex situ studies of carbon materials, the ratio of the D-band to G-band integrals (D/G ratio) is frequently used as a measure for lattice disorder and defects[17] or crystallite size.[18] However, the D-band disappears early during intercalation due to lithium insertion into defects and surface passivation due to solid electrolyte interphase (SEI) formation.[8,19] Thus, the determination of the D/G ratio is not suitable for the study of changes in the graphite electrode structure during battery cycling.

A number of studies on the impact of different sample properties and experimental conditions on Raman signal widths can be found in the literature. The effect of crystallite size was investigated for a variety of materials, where an inverse correlation to signal widths has been found and linked to phonon confinement as well as to compressive stress.[20–23] Size effects mainly occur for nanoparticles. Pressure was shown to increase Raman signal widths if applied anisotropically or if causing lattice defects or phase changes in the material.[21,24,25] For silicon, it was also demonstrated that the full-width-at-half-maximum (FWHM) of the characteristic signal at 520 cm^{-1} can be utilized to monitor lattice strains and defects.[26,27] For graphite materials specifically, Yoshida et al. investigated common origins for increases in D/G ratio and Raman signal widths.[28]

In the present work, Raman signal widths were analyzed for the in operando investigation of lithium intercalation into graphite. The suitability of the G-band FWHM as a substitute for the D/G ratio to study the disorder of graphite during battery cycling is examined.

2 | MATERIALS AND METHODS

All Raman measurements were carried out using a Bruker Senterra Raman microscope (Bruker, Germany). Experiments were performed using a 532 nm green laser at a spectral resolution of 9 to 18 cm^{-1} and a confocal setup. The laser power was set to 10 mW to prevent sample damage. The D/G ratio was derived by integrating the G-band and D-band signals. The G-band FWHM was determined by fitting the signal to a Voigt peak shape.

For reference measurements, Highly Oriented Pyrolytic Graphite (HOPG) (GoodFellow, Germany) and graphite powder with a mean particle size of 19–28 µm (Aldrich, Germany) were used. HOPG was prepared by removing the top graphene layer with adhesive tape to obtain a clean surface. During Raman experiments, only the basal plane of HOPG was studied. Fifty milligrams of graphite powder was pressed to a pellet with a diameter of 10 mm at 30 kN to achieve a smooth graphite surface. All material surfaces were scanned by recording multiple Raman spectra pointwise on a grid with an isotropic spatial resolution of 1 µm using a 100× magnification (25 × 20 points for HOPG, 35 × 35 points for the graphite pellet).

For *in operando* measurements a lithium versus graphite half-cell was set up inside an ECC-Opto-Std (EL-CELL, Germany) cell.[8] A lithium metal disk (Alfa, USA) of 1 mm thickness and a diameter of 10 mm was used as a counter electrode. A 1 mm thick glass fiber separator (EL-CELL, Germany) soaked with ca. 5 µL of LP30 electrolyte (1 M $LiPF_6$ in a 1:1 mixture of dimethyl carbonate and ethyl carbonate) (BASF, Germany) was placed on top of the lithium electrode. As working electrode, 3.73 mg graphite powder (Aldrich, Germany) was distributed on top of the separator and pressed onto the glass window of the cell.

The cell was cycled at a constant rate of 50 µA (C/15) between 0.001 V and 3.0 V using a BioLogic SP-200 potentiostat (BioLogic Science Instruments, France). During cycling, Raman spectra were recorded with a time step of 10 minutes at the center of a graphite particle of the graphite electrode with an isotropic spatial resolution of 2 µm (50× magnification).

3 | RESULTS

3.1 | Reference measurements on HOPG and graphite powder

Figures 1A–C show the distribution of the D/G ratio and the G-band FWHM across the HOPG surface. Both parameters yield similar information regarding the surface structure and represent comparable qualitative characteristics of the HOPG surface. Overall, regions with a high D/G ratio also feature a high FWHM. As the D/G ratio is mainly affected by lattice defects, it suggests that the FWHM too is impacted by local deformations of the graphite structure. However, the large surface defect (marked in gray in Figure 1) reveals areas with a low D/G ratio but medium to high FWHM. In this area of the HOPG surface, clusters of small crystal particles exist that cause an increase in signal widths in addition to an increase driven by local lattice

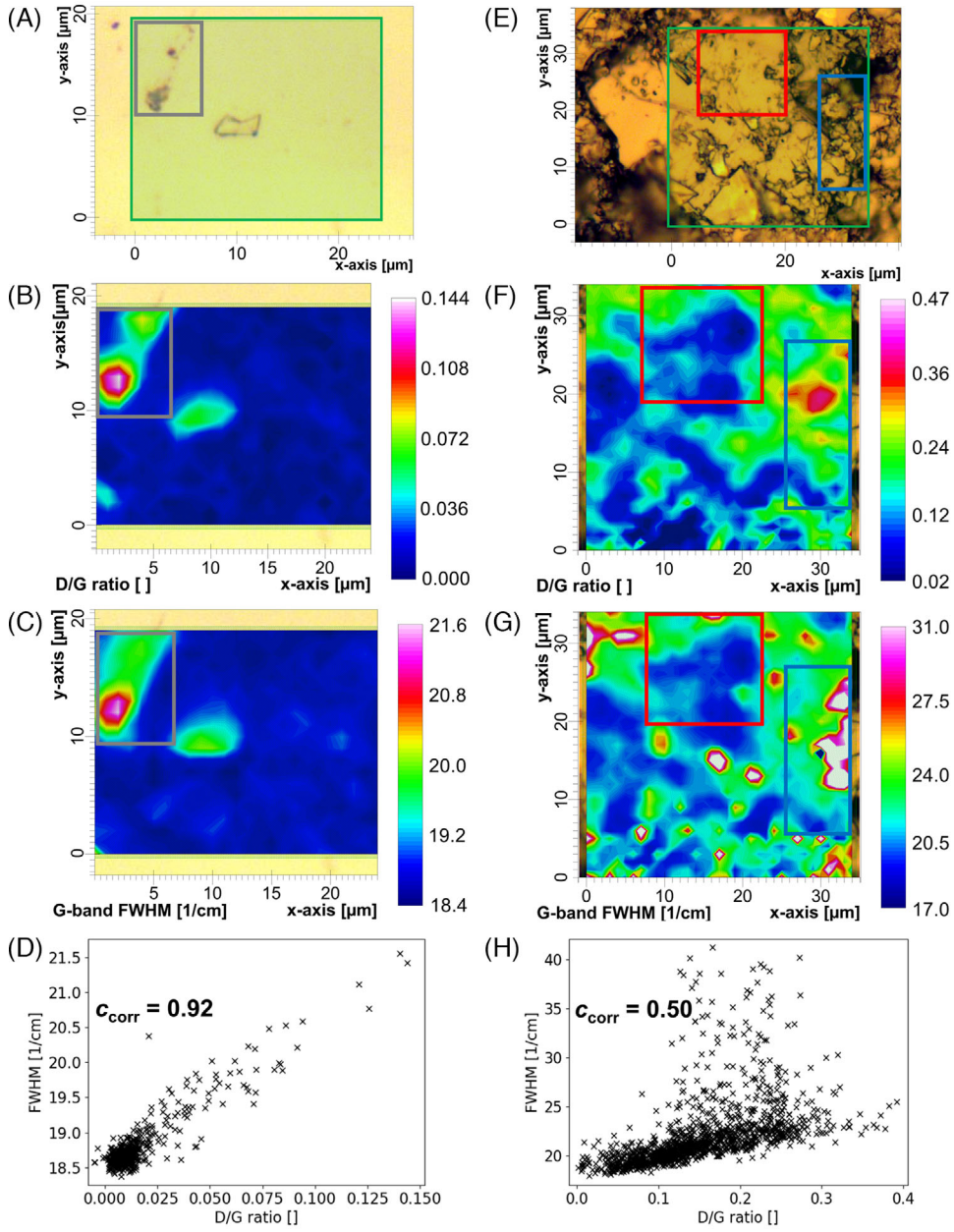

FIGURE 1 Microscopic images of HOPG (A) and the graphite powder pellet (E). Areas investigated by Raman microscopy are marked in green, regions of interest in gray, red, and blue. Pseudocolor plots of the D/G ratio for HOPG (B) and the graphite pellet (F). Pseudocolor plots of the G-band FWHM for HOPG (C) and the graphite pellet (G). Correlations between D/G ratio and FWHM for HOPG (D) and the graphite pellet (H)

defects.[20,22,25] For this sample, a high Pearson product-moment correlation coefficient c_{corr} = 0.92 between D/G ratio and G-band FWHM (Figure 1D) was determined.

In contrast to HOPG, the graphitic powder sample consists of a mixture of large and small crystallite particles (Figure 1E). While the basic features of the graphite powder surface can be displayed by both D/G ratio and the FWHM, there are multiple areas where high FWHM exists for low to medium D/G ratio (Figures 1F and 1G). It is likely that in addition to local lattice defect concentration, the FWHM is affected by the distribution of particles with low crystallite sizes. This is pronounced in the area marked in blue, where a large quantity of small particles are lumped together. The statistical linear correlation coefficient between the FWHM and the D/G ratio decreases to 0.50. However, Figure 1H reveals that most measurement points follow a linear correlation between both parameters, but there are notable exceptions that decrease the correlation factor significantly. Large graphite particles (marked in red) follow the linear correlation between the

Short Communication
doi.org/10.1002/elsa.202100068
Chemistry Europe
European Chemical Societies Publishing

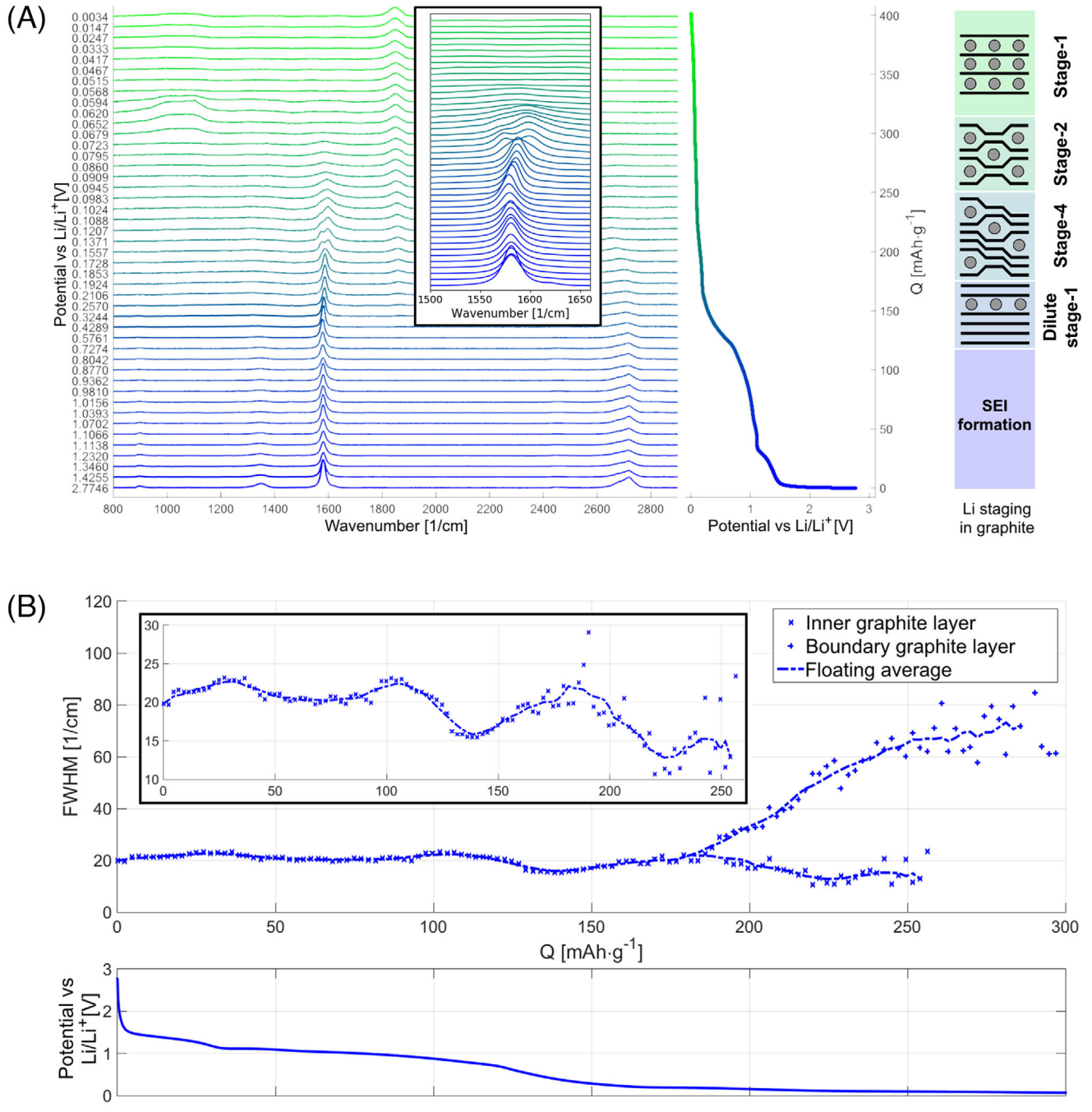

FIGURE 2 (A) In operando Raman spectra for the lithium-graphite half-cell under discharging conditions. The potential curve is shown on the right together with the proposed intercalation stages. (B) Evolution of the FWHM of the G-band during discharge. The box in the top left shows a magnification of the bottom part of the FWHM. The potential versus time curve is given in the bottom panel

D/G ratio and the FWHM, and are mainly influenced by lattice deformation and defects.[22]

It can be concluded that the FWHM of the G-band can be a feasible substitute for the D/G ratio for structure analysis of carbon materials if measurement conditions are carefully chosen. For single graphite particles or large graphitic structures such as HOPG, the effect of particle clusters with small and varying crystallite sizes on the FWHM is negligible and a linear correlation between D/G ratio and G-band FWHM can be assumed.

3.2 | In operando Raman spectroscopy of the lithium vs. graphite half-cell

Figure 2A shows the potential curve of the discharge cycle together with the corresponding Raman spectra. From

the onset of the discharge until 0.7 V (119 mAh/g) an SEI is formed and the D-band vanishes.[29] Up to 198 mV (167 mAh/g) lithium is inserted stochastically into the lattice, denoted as dilute stage-1. With the onset of lithium intercalation, the G-band intensity decreases due to the increased conductivity of the intercalation compound. Furthermore, the G-band blueshifts to 1590 1/cm as intercalation increases the force constants of graphite lattice bonds.[5,8] Afterwards, staged intercalation compounds are formed, which are observable as peak splitting of the G-band. Three plateaus can be observed at 198-186 mV (167-180 mAh/g), 110–83 mV (225-277 mAh/g), and 70-62 mV (296-333 mAh/g), which coincide with the formation of stage-4, stage-2, and stage-1 intercalation compounds, respectively.[16,30]

The peak splitting of the G-band originates from the presence of inner and boundary graphite layers upon the formation of the stage-4 compound.[5,8] Boundary layers refer to charged graphite layers in direct contact with intercalated ions, while the inner layers are sandwiched between graphite sheets without adjacent ions and remain largely unchanged. The number of inner layers as well as their corresponding signal decreases over time and vanishes for the formation of the stage-2 compounds. The onset of G-band splitting can be identified most sensitively as the point where the line cannot be fitted to a single peak. During the formation of the stage-1 compound, the G-band disappears, which is suggested to be caused by the low penetration depth of the laser due to the high conductivity of LiC_6.[5] Additional signals were found at 1050 cm^{-1} and 1850 cm^{-1}, for which we refer to ref. 31.

These observations are in agreement with intercalation studies in the literature.[5,11,14–16] However, additional information about the intercalation process can be gained by analyzing the G-band signal width, which is impacted by local lattice deformation due to intercalation and the resulting lattice defects. Other factors that influence the FWHM, such as changes in crystallite size and in pressure, can be neglected in this study. No external pressure was applied to the battery. Raman spectra were recorded in the center of a graphite particle with 15–20 μm in diameter. Crystalline particles of this size are not known to affect Raman signal widths. Moreover, the size of the particle stayed constant during the experiment, except for small volume changes on the order of 4%.

Figure 2B shows the evolution of the G-band FWHM during the discharge of the battery. During the formation of the SEI layer (up to 70 mAh/g) and the formation of a dilute stage-1 (70–167 mAh/g) an oscillation of the signal width was observed. The amplitude of the oscillation increases after the SEI formation is completed. The repeated increase and decrease in signal width correspondingly suggests an intercalation process during dilute stage-1 where phases of high lattice deformation are followed by phases of relaxation. This indicates that intercalation evolves not completely continuously and homogeneously. The presence of changes in the graphite signal width during SEI formation implies that intercalation already takes place from the beginning of the discharge process, albeit to a low extent due to the small oscillation amplitude. Moreover, a reversible increase in FWHM during intercalation is likely attributed to localized biaxial strain experienced by the graphene layers due to an increase in C-C bond length.[32,33] By contrast, intercalation-induced lattice defects are non-reversible and would contribute to a permanent increase in FWHM.

Starting with the formation of the stage-4 compound (167 mAh/g), the signal widths of both the boundary and inner layer have to be considered. The FWHM of the inner layer slightly decreases. The lack of an increase in the inner layer signal width confirms the notion that these layers remain largely unchanged compared to pristine graphene layers.[32,33] The slight decrease the inner layer FWHM may be caused by the blockage of phonon decay channels.[34] Simultaneously, the FWHM of the boundary layer significantly increases from *ca*. 20 to 100 cm^{-1}. It indicates a continuous, local deformation of the graphene layers in contact with the lithium ions, which increases the C-C bond length and induces biaxial strain on the graphene sheet. No plateau or decrease in the evolution of the boundary layer signal FWHM could be observed, suggesting that no staged GICs with nondeformed boundary graphene sheets exist, as predicted, e.g. by the Rüdorff model of intercalation. In contrast, the intercalation process hardly affects the signal FWHM of the inner layer and thus there is no evidence for deformation. Due to the disappearance of the G-band for stage-1, no prediction for the fully intercalated compound can be made.

During charging of the battery, the G-band FWHM returns to its original value at 20 cm^{-1}. From stage-1 to stage-4, the FWHM exhibits an identical, but reverse evolution. Contrary to the discharging process, no repeated increase and decrease in FWHM is observed during the dilute stage-1. The reversible behavior of the FWHM indicates that the changes in signal width are due to elastic deformation and not the formation of lattice defects during the first cycle intercalation. However, different mechanisms may be present during later cycles of intercalation and deintercalation.

4 | CONCLUSIONS

It has been shown that the FWHM of the graphite G-band correlates with the D/G ratio if other properties such as

crystallite size or pressure can be neglected. Therefore the G-band FWHM can be employed to describe the deformation in graphite electrodes during lithium intercalation. The analysis of the G-band signal width during intercalation can thus be regarded as an additional measure for the interpretation and modeling approaches of intercalation processes. It was shown that relative changes in FWHM at a single sample position are more sensitive to structural alterations in comparison to absolute line widths at multiple positions. During the in operando study of a lithium versus graphite cell, the evolution of the FWHM suggested that intercalation already takes place to a small extent during SEI formation. Further, the formation of the staged intercalation compounds leads to a continuous deformation of the boundary graphene layer of intercalated graphite.

ACKNOWLEDGMENTS

This work was supported by the Federal Ministry of Education and Research as part of the research cluster "Aqua" within the project InOPlaBat (grant number 03XP0352).

CONFLICT OF INTEREST

The authors declare no conflict of interest.

DATA AVAILABILITY STATEMENT

The data that support the findings of this study are available from the corresponding author upon reasonable request.

ORCID

Sven Jovanovic https://orcid.org/0000-0002-1227-4936
Peter Jakes https://orcid.org/0000-0002-5187-4969
Steffen Merz https://orcid.org/0000-0002-2163-5027
Rüdiger-A. Eichel https://orcid.org/0000-0002-0013-6325
Josef Granwehr https://orcid.org/0000-0002-9307-1101

REFERENCES

1. J. R. Dahn, R. Fong, M. J. Spoon, *Phys. Rev. B Condens. Matter* **1990**, *42*, 6424.
2. R. Fong, U. Vonsacken, J. R. Dahn, *J. Electrochem. Soc.* **1990**, *137*, 2009.
3. J. R. Dahn, A. K. Sleigh, H. Shi, J. N. Reimers, Q. Zhong, B. M. Way, *Electrochim. Acta* **1993**, *38*, 1179.
4. M. Winter, J. O. Besenhard, M. E. Spahr, P. Novák, *Adv. Mat.* **1998**, *10*, 725.
5. M. Inaba, *J. Electrochem. Soc.* **1995**, *142*, 20.
6. M. Endo, C. Kim, K. Nishimura, T. Fujino, K. Miyashita, *Carbon* **2000**, *38*, 183.
7. S. Klamor, K. Zick, T. Oerther, F. M. Schappacher, M. Winter, G. Brunklaus, *Phys. Chem. Chem. Phys.* **2015**, *17*, 4458.
8. C. Sole, N. E. Drewett, L. J. Hardwick, *Faraday Discuss.* **2014**, *172*, 223.
9. M. D. Levi, E. A. Levi, D. Aurbach, *J. Electroanal. Chem.* **1997**, *421*, 89.
10. Y. Li, Y. Lu, P. Adelhelm, M. M. Titirici, Y. S. Hu, *Chem. Soc. Rev.* **2019**, *48*, 4655.
11. M. S. Dresselhaus, G. Dresselhaus, *Adv. Phys.* **2002**, *51*, 1
12. F. Tuinstra, J. L. Koenig, *J. Chem. Phys.* **1970**, *53*, 1126.
13. J. Maultzsch, S. Reich, C. Thomsen, H. Requardt, P. Ordejon, *Phys. Rev. Lett.* **2004**, *92*, 075501.
14. L. J. Hardwick, P. W. Ruch, M. Hahn, W. Scheifele, R. Kötz, P. Novák, *J. Phys. Chem. Solids* **2008**, *69*, 1232.
15. G. Fredi, S. Jeschke, A. Boulaoued, J. Wallenstein, M. Rashidi, F. Liu, R. Harnden, D. Zenkert, J. Hagberg, G. Lindbergh, P. Johansson, L. Stievano, L. E. Asp, *Multifunct. Mater.* **2018**, *1*, 015003.
16. V. A. Sethuraman, L. J. Hardwick, V. Srinivasan, R. Kostecki, *J. Power Sources* **2010**, *195*, 3655.
17. S. N. Behera, S. M. Bose, S. N. Behera, B. K. Roul, *AIP Conf Proc.* **2008**, *1063*.
18. P. Mallet-Ladeira, P. Puech, C. Toulouse, M. Cazayous, N. Ratel-Ramond, P. Weisbecker, G. L. Vignoles, M. Monthioux, *Carbon* **2014**, *80*, 629.
19. E. Peled, *J. Electrochem. Soc.* **1979**, *126*, 2047.
20. V. Swamy, A. Kuznetsov, L. S. Dubrovinsky, R. A. Caruso, D. G. Shchukin, B. C. Muddle, *Phys. Rev. B* **2005**, *71*.
21. J. W. Ager 3rd, D. K. Veirs, G. M. Rosenblatt, *Phys. Rev. B Condens. Matter* **1991**, *43*, 6491.
22. K. Nakamura, M. Fujitsuka, M. Kitajima, *Phys. Rev. B Condens. Matter.* **1990**, *41*, 12260.
23. M. Lazzeri, S. Piscanec, F. Mauri, A. C. Ferrari, J. Robertson, *Phys. Rev. B* **2006**, *73*, 155426.
24. C. Ulrich, A. Debernardi, E. Anastassakis, K. Syassen, M. Cardona, *Phys. Status Solidi B* **1999**, *211*, 293.
25. J. Schwan, S. Ulrich, V. Batori, H. Ehrhardt, S. R. P. Silva, *J. Appl. Phys.* **1996**, *80*, 440.
26. T. Wermelinger, R. Spolenak, *J. Raman Spectrosc.* **2009**, *40*, 679.
27. D. Beeman, R. Tsu, M. F. Thorpe, *Phys. Rev. B Condens. Matter* **1985**, *32*, 874.
28. A. Yoshida, Y. Kaburagi, Y. Hishiyama, *Tanso* **2006**, *2006*, 2.
29. P. Novák, F. Joho, M. Lanz, B. Rykart, J.-C. Panitz, D. Alliata, R. Kötz, O. Haas, *J. Power Sources* **2001**, *97–98*, 39.
30. T. Ohzuku, Y. Iwakoshi, K. Sawai, *ChemInform* **2010**, *24*.
31. M. A. Cabañero, M. Hagen, E. Quiroga-González, *Electrochim. Acta* **2021**, *374*, 137487.
32. J. C. Chacon-Torres, L. Wirtz, T. Pichler, *Phys. Status Solidi B* **2014**, *251*, 2337.
33. J. C. Chacon-Torres, L. Wirtz, T. Pichler, *ACS Nano* **2013**, *7*, 9249.
34. A. Das, S. Pisana, B. Chakraborty, S. Piscanec, S. K. Saha, U. V. Waghmare, K. S. Novoselov, H. R. Krishnamurthy, A. K. Geim, A. C. Ferrari, A. K. Sood, *Nat. Nanotechnol.* **2008**, *3*, 210.

How to cite this article: S. Jovanovic, P. Jakes, S. Merz, R.-A. Eichel, J. Granwehr, *Electrochem. Sci. Adv.* **2022**, *2*, e2100068. https://doi.org/10.1002/elsa.202100068